



Three distinct circulation patterns that induce enhanced intraseasonal precipitation events over South China in boreal winter

Lu Wang^{1,2} · Jie Jiang^{1,3} · Tim Li^{1,4} · Xuan Zhou¹ · Ziqi Chen¹

Received: 24 December 2021 / Accepted: 21 August 2022 / Published online: 6 September 2022
© The Author(s), under exclusive licence to Springer-Verlag GmbH Germany, part of Springer Nature 2022

Abstract

This study identified three distinct circulation patterns that induce enhanced intraseasonal precipitation events (IPEs) over South China (SC) in boreal winter based on observational data of 1979–2016. The three categories account for 45%, 33% and 14% of total IPEs, respectively. In Category I, a cyclonic anomaly with quasi-barotropic vertical structure propagates southward from the northern Asia while no signal of the Madden–Julian Oscillation (MJO) is observed. Category II (III) is featured by a fast (slow)-propagating MJO that shows suppressed (enhanced) convection over the equatorial western Pacific (Maritime Continent) during the peak-wet phase of SC. The common process responsible for the onset of IPEs is boundary-layer moistening dominated by mean moisture advection due to intraseasonal southerly wind. For Category I, the anomalous southerly arises from the southwesterly to the southeast of the mid-latitude cyclone. For Category II, it is attributed to the southwesterly to the west of the anticyclone over the northwestern Pacific, as a response to the suppressed MJO convection over the western Pacific. For Category III, it is due to the southwesterly to the east of the cyclone over India in response to the enhanced MJO convection over the eastern Indian Ocean. The moisture origins for the three categories are also distinguishable.

1 Introduction

In boreal winter, most parts of the eastern China are characterized by dry and cold conditions as influenced by the East Asian winter monsoon, whereas South China (SC) has abundant precipitation due to ample moisture. In the recent past years, several extreme wet winters occurred over SC such as the beginning of 2008 and 2010, causing extensive damage and serious direct economic losses (e.g., Tao and

Wei 2008; Yao and Huang 2016). These extreme cases were all featured by long-lasting precipitation, closely related to atmospheric intraseasonal oscillations (Hong and Li 2009; Wu et al. 2009; Yao et al. 2014). It is estimated that the intraseasonal precipitation variance accounts for roughly 50% of the total over SC during boreal winter (Yao et al. 2020). However, the current state-of-the-art forecasting systems show very low sub-seasonal prediction skill of it (e.g., Liu et al. 2022). It may be partially due to lack of understanding the critical circulation systems responsible for the onset of precipitation.

Numerous studies have identified that the Madden–Julian oscillation (MJO) (Madden and Julian 1972; Li et al. 2020), characterized by slow eastward propagating deep convection along the equator, exerts a great influence on intraseasonal precipitation over SC (e.g., Jia et al. 2011; Jeong et al. 2008; Li et al. 2014; Cui and Li 2021; Liu et al. 2020). During the MJO phases 2 and 3 [as defined by Wheeler and Hendon (2004)] when the enhanced (suppressed) MJO convection is located over the eastern Indian Ocean (western Pacific), the SC precipitation tends to significantly increase; whereas during the MJO phases 6 and 7 when the enhanced MJO convection is over the western Pacific, the SC precipitation decrease.

✉ Lu Wang
luwang@nuist.edu.cn

- ¹ Key Laboratory of Meteorological Disaster, Ministry of Education (KLME)/Collaborative Innovation Center on Forecast and Evaluation of Meteorological Disasters (CIC-FEMD)/Joint International Research Laboratory of Climate and Environment Change (ILCEC), Nanjing University of Information Science and Technology, Nanjing 210044, China
- ² Laboratory for Regional Oceanography and Numerical Modeling, Qingdao National Laboratory for Marine Science and Technology, Qingdao, China
- ³ Nantong Meteorological Bureau, Nantong, China
- ⁴ International Pacific Research Center, University of Hawai‘i at Mānoa, Honolulu, USA

Several physical processes have been proposed to explain the intraseasonal modulation of precipitation over East Asia by the MJO cycle. The first way is through modulating lower-level moisture transport (e.g., Ren and Ren 2017). During MJO phases 2–3 (phases 6–7), anomalous moisture convergence (divergence) due to intraseasonal southwesterly (northeasterly) wind in the lower troposphere is found over SC, which is conducive to positive (negative) rainfall anomaly (Jia et al. 2011). The southwesterly anomaly during MJO phases 2–3 may be related to the simultaneous enhancement of the trough over the Bay of Bengal (BoB) (Wang et al. 2011) and the western Pacific (WP) subtropical high (Zong et al. 2014). The second way is through upper-level Rossby wave trains from the tropics to the midlatitudes, which are triggered by MJO diabatic heating (Liu and Yang 2010; Zhang 2013). In response to the enhanced convection over the eastern Indian Ocean (IO) during MJO phases 2–3, a pair of anticyclonic anomalies in upper troposphere are excited symmetric about the equator west of the heating (Gill 1980), and the northern one over the Arabian Sea in turn induces a northeastward-propagating Rossby wave train to the midlatitudes. The wave train consists of an anomalous cyclone over China and an anomalous anticyclone over the middle of Japan; the cyclonic one is conducive to precipitation over SC (Hung et al. 2014). With the eastward propagation of MJO heat source, the wave train shifts eastward. In addition, the MJO convection could impact SC through inducing meridional overturning circulation or local Hadley circulation (He et al. 2011; Seo et al. 2016; Peng et al. 2019; Chen et al. 2021a, b).

Some more recent studies suggested the crucial role of the middle-and-high latitude intraseasonal oscillation (ISO) in modulating the SC intraseasonal precipitation (e.g., Yao et al. 2015; Yao et al. 2020; Stan et al. 2017; Chen et al. 2021a; Zhu and Yang 2021). Yao et al. (2020) analyzed the intraseasonal circulation evolutions composited for all the intraseasonal precipitation events (IPEs) over SC in boreal winters from 1979 to 2013. They suggested that the precipitation variation is mainly due to moisture accumulation (loss) induced by intraseasonal southerly (northerly) wind in the lower troposphere. The appearance of intraseasonal southerly (northerly) wind over SC is related to a southward propagating low-level cyclonic (anticyclonic) anomaly from polar region, while no clear signal of the MJO in the tropics is seen in their study. Using the real-time multivariate MJO (RMM) indices (Wheeler and Hendon 2004) to reconstruct the precipitation anomaly, Yao et al. (2015) showed that only 10% of the total subseasonal precipitation variability in SC is accounted for by the MJO. The rest variabilities are primarily due to cold surge phenomenon or the development of a Siberian high and cold-air outbreak in East Asia associated with a wave train from the North Atlantic (Park et al. 2014; Kim et al. 2020).

The lack of consensus in terms of the key circulation systems responsible for the enhanced IPEs over SC may suggest the diversity of precipitation origins. However, a systematic and objective delineation of the diversified circulations and related mechanisms that explain the onset of SC intraseasonal precipitation events have not yet emerged. In this study, we propose a way to objectively classify the SC enhanced IPEs, as well as to reveal different circulation patterns in each type. The results are expected to advance our understanding of the precursors of SC precipitation and to improve its simulation and prediction.

The remainder of this study is organized as follows. Section 2 describes the data and methods and Sect. 3 presents the categorization results of detected SC IPEs. In Sect. 4, the dominant moisture processes that induce precipitation anomalies are revealed and their origins in different categories are explored in Sect. 5. The conclusions and discussion are shown in Sect. 6.

2 Data and methods

2.1 Data

Daily high-resolution ($0.25^\circ \times 0.25^\circ$) gridded precipitation data from the CN05.1 dataset (Wu and Gao 2013) provided by the National Climate Center in China is used to identify SC IPEs. Daily winds, geopotential height and specific humidity are obtained from the ERA-interim dataset (Dee et al. 2011) at $1.5^\circ \times 1.5^\circ$ spatial resolution. Daily outgoing longwave radiation (OLR) data (Liebmann and Smith 1996) with $2.5^\circ \times 2.5^\circ$ produced by National Oceanic and Atmospheric Administration (NOAA) polar-orbiting satellites is utilized to represent tropical convections. All data used here are extracted for the same period of 1979–2016 and only the boreal winter season [November–March (NDJFM)] is focused on in current analysis.

2.2 Selecting the SC enhanced IPEs

Considering that the spectrum peak of SC precipitation is mainly observed in 10–30-day band (Yao et al. 2020) and that of MJO is in 30–60-day band (Madden and Julian 1972), here a 10–70-day bandpass filter (Duchon 1979) is applied to the daily precipitation and other variables to extract the intraseasonal anomalies. Prior to filtering, all fields are removed of the annual cycle. It is worth mentioning that we also tried the 10–30-day bandpass filter, and found similar results as shown in the following study.

Then, an intraseasonal precipitation index is constructed over SC [i.e., (22° – 30° N, 110° – 120° E)] where maximum intraseasonal precipitation variance is found (Yao et al. 2020). An enhanced IPE is identified when the precipitation

Table 1 List of days and regions selected for the cluster analysis

Days	Regions
Day 0	20° N–20° E, 30°–180° E
Day – 3 to day 3 average	20° N–20° E, 30°–180° E
Day – 2 to day 2 average	30° N–30° E, 30°–180° E
Day – 2 to day 2 average	20° N–20° E, 40°–160° E

index exceeds one standard deviation and the day with maximum precipitation is marked as day 0. According to this criteria, a total of 144 IPEs are selected in boreal winter from 1979 to 2016.

2.3 Cluster analysis

To classify the detected IPEs, we apply the *k*-means clustering analysis to the spatial (i.e., two-dimensional) distributions of intraseasonal OLR anomalies over the tropical Indo-western Pacific region near Day 0 of each event. Several different domains and date ranges, as shown in Table 1, are tested to perform the clustering analysis. Note that the OLR anomalies greater than -5 W m^{-2} and less than 5 W m^{-2} are set to zero and a nine-point (i.e., 3×3) local smoothing is performed to remove small-scale noises prior to clustering analysis, as did by Wang et al. (2019) who classified the MJO propagations. After categorization, composite analysis is conducted for each group, and one-sided Student’s *t*-Test is applied to show the significant results. The degree of freedom for a given group is estimated as $n-1$, where n denotes the number of events in the group.

2.4 Moisture budget analysis

The intraseasonal moisture tendency equation is written as follows (Hsu and Li 2012):

$$\frac{\partial q'}{\partial t} = -\left(u \frac{\partial q'}{\partial x}\right)' - \left(v \frac{\partial q'}{\partial y}\right)' - \left(\omega \frac{\partial q'}{\partial p}\right)' - \left(\frac{Q_2}{L}\right)' \quad (1)$$

where q is the specific humidity, u the zonal wind, v the meridional wind, ω the vertical pressure velocity, Q_2 the atmospheric apparent moisture sink, and L the latent heat of condensation. A prime denotes the intraseasonal component. On the right-hand side of Eq. (1), the first term represents zonal moisture advection, the second term meridional moisture advection, the third term vertical moisture advection, and the fourth term moisture sink.

A variable can be further decomposed into three components according to the timescales: the low-frequency background state that includes the annual cycle (LFBS, with a period > 70 days), intraseasonal component, and

higher-frequency (with a period < 10 days) component. Thus, the meridional moisture advection term could be written as

$$-\left(v \frac{\partial q'}{\partial y}\right)' = -\left(\bar{v} \frac{\partial \bar{q}'}{\partial y}\right)' - \left(v' \frac{\partial \bar{q}}{\partial y}\right)' - \left(v' \frac{\partial q'}{\partial y}\right)' - \left(v'^* \frac{\partial q^*}{\partial y}\right)' \quad (2)$$

where the overbar, prime, asterisk denote the LFBS, intraseasonal and higher-frequency components, respectively.

3 Categorization of SC IPEs

To obtain optimal classified results, we have tried to set different cluster number k . It is found that the identified IPEs can be optimally clustered into three groups in which the silhouette values are all greater than 0.1, while the non-clustered events with silhouette values less than 0.1 constitute a new group. When k increases, the number of non-clustered events increases (figure not shown).

Figure 1 displays the proportion of events in the Non-clustered, Cluster 1 and Cluster 2 groups, respectively. They are the top three categories, which make up the majority of total events. Cluster 3 is not shown because it has very few events, and on the other hand, this group is not associated with MJO or any other well-known mode of tropical convection (figures not shown). The markers represent the results obtained by slightly changing analyzed domain and date range as shown in Table 1, while the bars denote the average. Note that only small variations of the case numbers in each group are found, indicating the robustness of current classification. On average, the three groups account for 45%, 33% and 14% of the total events respectively. For convenience, they are referring to be Categories I, II and III respectively hereinafter.

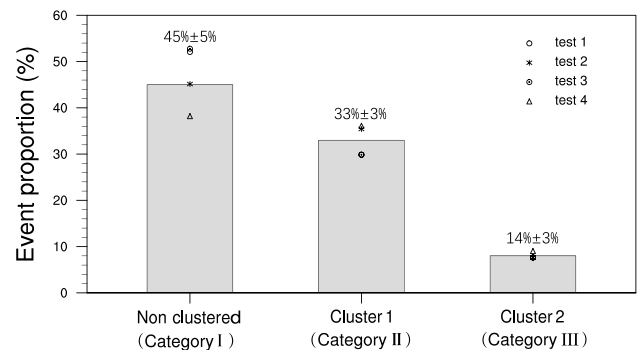


Fig. 1 Proportion of SC intraseasonal precipitation events to the total events for each cluster. Markers denote the results based on different calculations listed in Table 1, while the bars represent the average. The averaged proportion value and its variation range for each cluster are marked on top of each bar

The life cycles of SC intraseasonal precipitation anomalies in the three categories are compared in Fig. 2. Note that the cluster result derived from one test (i.e., day -2 to day $+2$ averaged OLR anomalies over 20°S – 20°N , 40°E – 160°E) is presented as a representative in the current analysis. As is shown, the precipitation evolutions resemble each other very much, with days $+7$ and -7 being the driest phase and day 0 the peak wet phase. It suggests that the dominant period of SC intraseasonal precipitation is two weeks. Furthermore, all the precipitation anomalies change from negative to positive near day -4 , indicating the onset of precipitation. The horizontal evolutions of precipitation anomalies are consistent with the area-averaged results. As shown in Fig. 3, the three categories show very similar horizontal patterns of precipitation anomalies that are confined over SC, albeit with slight difference in amplitude. One may note that the negative precipitation anomalies on days $+7$ and -7 are much weaker than the positive precipitation anomaly on day 0. It should be due to the broad intraseasonal spectrum of rainfall anomalies. Assuming that one event has a period of 13 days and the other has a period of 17 days, their composite results would show minimum precipitation on days $+7$ and -7 , but the amplitude would be weakened. As the current study mainly focuses on the enhanced precipitation events, the weakened precipitation amplitude on days with minimum rainfall would not affect our results.

Then, the tropical convective anomalies in each category are examined. The left panels of Fig. 4 display horizontal patterns of intraseasonal OLR anomalies on day 0 for each group and the right panels show their zonal evolutions from day -25 to day $+25$ along the equator (20°S – 20°N average). As expected, the tropical convective anomalies are very weak and scattered in Category I (Fig. 4a), and no systematic propagation can be observed (Fig. 4b). It suggests that this

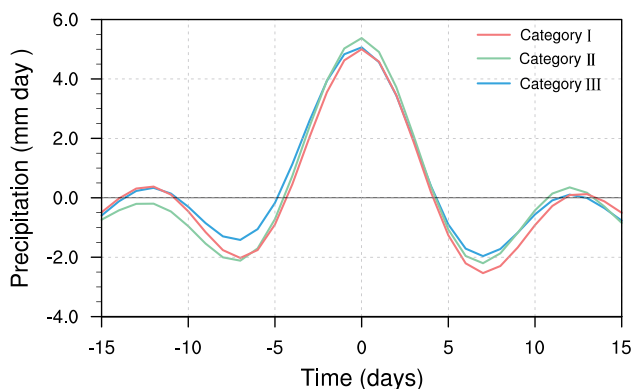


Fig. 2 Evolutions of intraseasonal rainfall anomalies (mm day^{-1}) averaged over SC (22 – 30°N , 110 – 120°E) from day -15 to day $+15$ composite for precipitation events in Category I (red), Category II (green) and Category III (blue)

category is not associated with MJO or other significant tropical intraseasonal convective anomalies.

In contrast, significant convective anomalies propagating eastward along the equator are observed in Categories II and III (Fig. 4d and f), indicating that both groups are accompanied by the MJO. But the MJO propagation speeds in the two clusters are obviously different. The phase speed is then estimated based on the Hovmöller diagram of enhanced convective anomaly using linear regression method. It shows that the MJO in Category II propagates at a speed about 6 m s^{-1} while that in Category III at a speed about 4 m s^{-1} . They both are the average from calculations based on different time spans of day -20 to day $+20$ and day -15 to day $+15$. According to the classification of MJO propagation by Wang et al. (2019), the MJO in Category II belongs to the fast-propagating type and that in Category III the slow-propagating type. In addition, the MJO phases are also different between the two clusters. In Category II, the OLR distribution on Day 0 is similar to MJO phases 2 and 3, with a suppressed convection near the WP and an enhanced convection over the IO (Fig. 4c). In Category III, it is similar to that of MJO phases 4 and 5, with an enhanced convection over the Maritime Continent (MC) and a suppressed one over the IO (Fig. 4e).

In summary, the observed enhanced SC IPEs can be primarily classified into three categories; the first one is not associated with MJO in tropics, and the other two are associated with two types of MJOs. Then, an interesting question arises as how the different intraseasonal circulations influence the precipitation over SC in each category? This question will be addressed in next two sections.

4 Dominant processes responsible for onset of precipitation

In this section, we will identify the critical processes for triggering precipitation through a moisture budget analysis. Figure 5 displays the evolutions of boundary-layer (BL; 1000 – 850 hPa) integrated intraseasonal moisture anomalies as well as their tendencies over SC for each category. The time series for the three categories show high similarities. On average, small positive BL moisture anomalies emerge on day -7 ; they increase and reach the peak on day -2 and then gradually dissipate. The moisture tendency anomalies precede the moisture variation 2–3 days. It is noted that the small positive BL moisture anomaly during days -7 to -5 is an essential component that leads to precipitation, as it could generate a potentially unstable stratification (e.g., Hsu and Li 2012). By contrast, the large positive moisture anomaly observed after the precipitation onset on day -4 is related to the column ascending motion resulted from precipitation (figure not shown). Thus, the specific processes that give rise to the positive

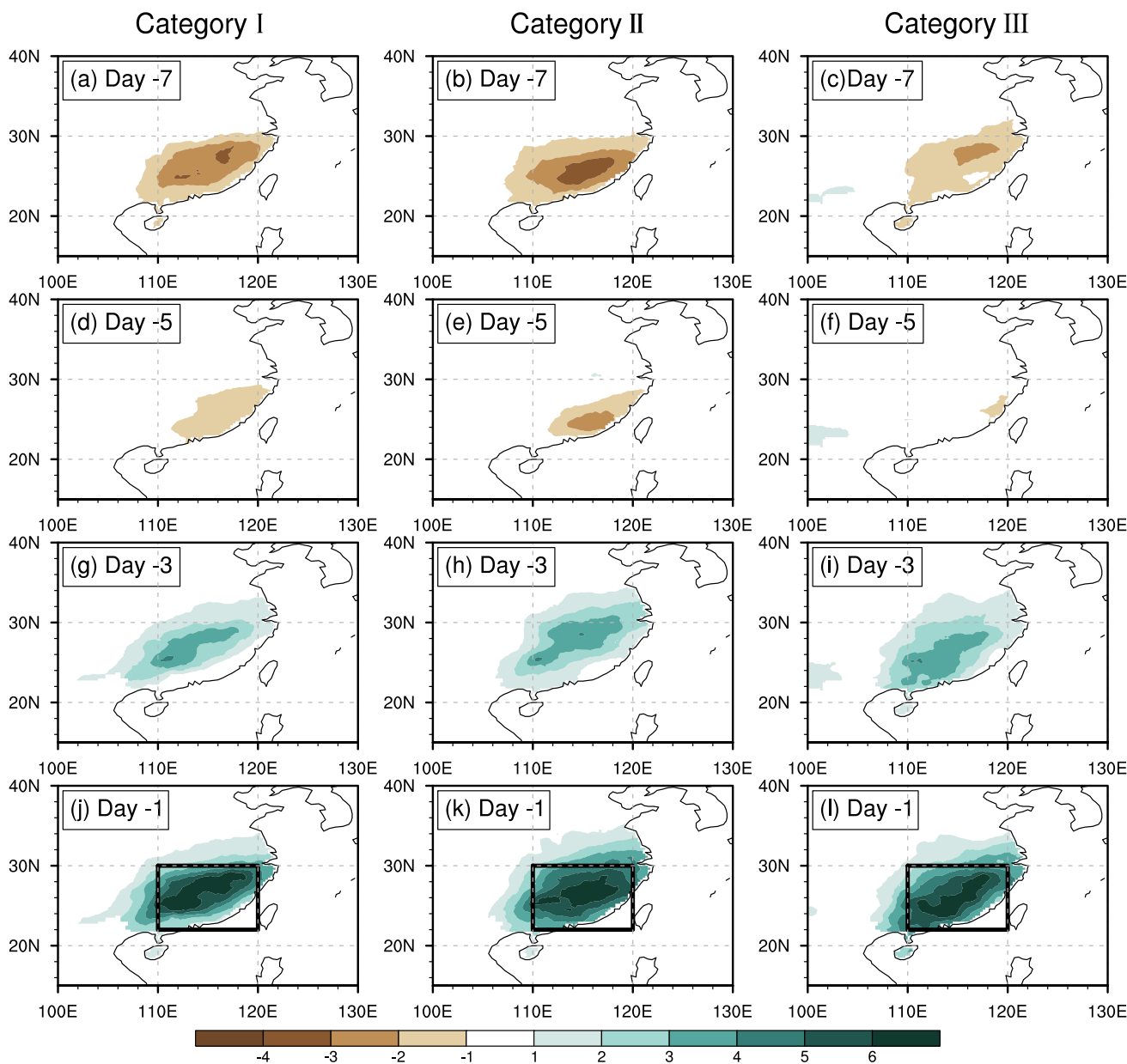


Fig. 3 Horizontal patterns of intraseasonal rainfall anomalies (mm day^{-1}) from day -7 to day -1 with an interval of 2 days for Category I, Category II and Category III. The rectangles in the bottom row denote the SC region

BL moisture tendency during the moistening phase (i.e., days -7 to -5) will be examined next.

Figure 6a displays the contribution from each moisture budget term as shown in Eq. (1) during the moistening phase. The positive moisture tendency mainly comes from the meridional moisture advection and $-\left(\frac{\partial_2}{L}\right)$, which show equal contributions, whereas the zonal and vertical advective play negative roles. As $-\left(\frac{\partial_2}{L}\right)$ is related to the condensational heating processes, the increase of moistening by $-\left(\frac{\partial_2}{L}\right)$ should be due to the intraseasonal descending motion anomaly (figure not shown) that suppresses raindrop-induced evaporation in the unsaturated atmosphere.

The meridional moisture advection term is further partitioned according to Eq. (2) to separate the effects from the basic state, intraseasonal perturbation and synoptic eddy (see Fig. 6b). Overall, this term in the three categories is dominated by the mean state moisture advection due to intraseasonal flow (i.e., $-\left(v' \frac{\partial \bar{q}}{\partial y}\right)$), which is induced by intraseasonal southerly wind advecting maximum mean moisture from the equatorial region northward. The anomalous moisture advection by background meridional wind also plays a positive role in Category III, but the reason is not clear. In short, the enhanced IPEs in the three categories

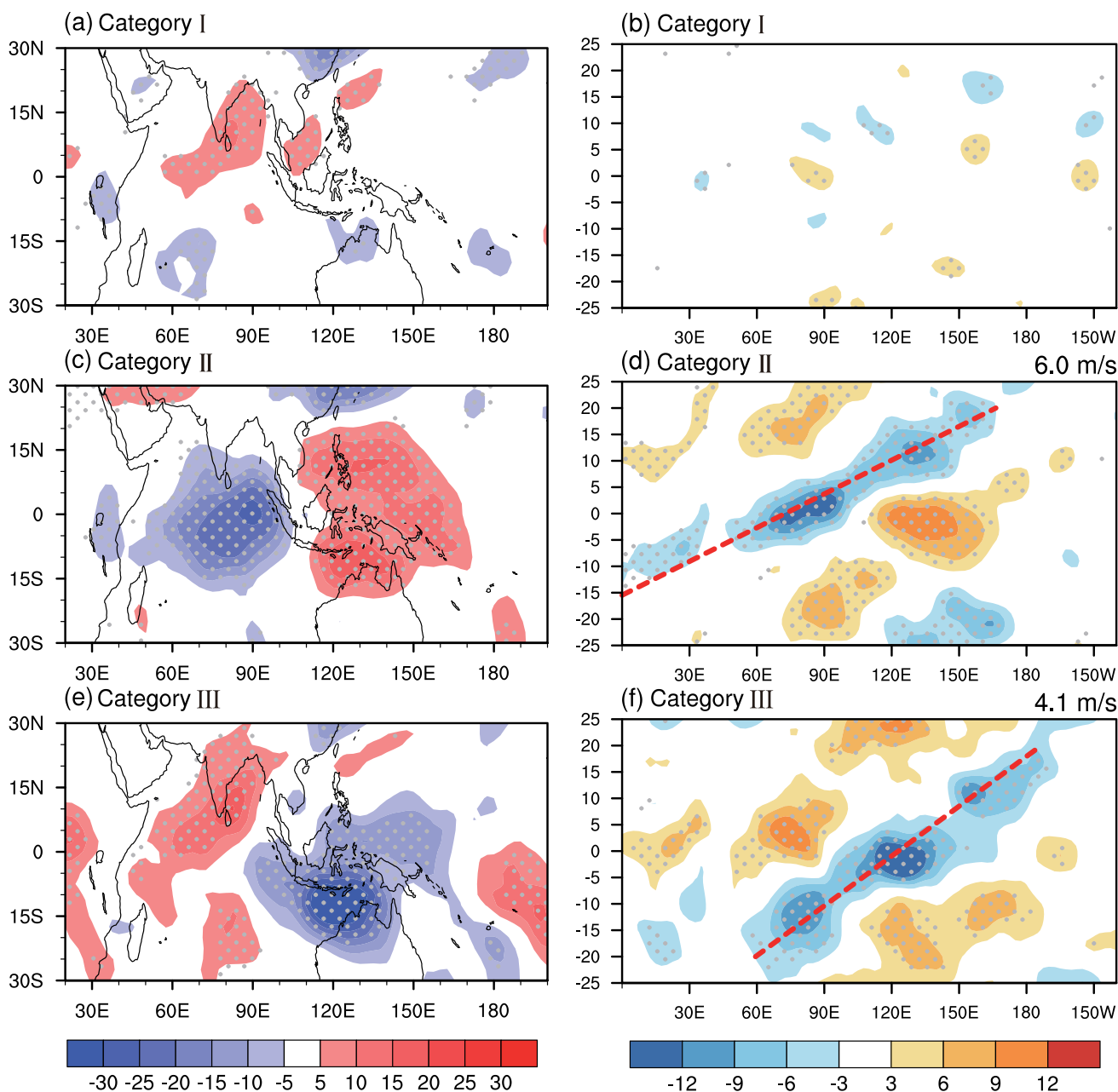


Fig. 4 Horizontal pattern of intraseasonal OLR anomalies ($W m^{-2}$) on day 0 and its zonal propagation along the equator ($20^{\circ} S-20^{\circ} N$ average) from day -25 to day $+25$ for **a, b** Category I, **c, d** Category II and **e, f** Category III, respectively. The regions exceeding the 95%

confidence level are stippled. The phase speed of the enhanced convective anomaly for Category II (Category III) is indicated on the top right corner of **(d)** [**f**] and the slope of the red dotted line denote the phase speed of $6 m s^{-1}$ ($4 m s^{-1}$)

are induced by a common pre-moistening process due to low-level southerly wind anomaly.

5 Different origins of low-level southerly wind in moistening phase

To understand the origin of the low-level southerly wind near SC in each category, we examine the evolutions of horizontal map of intraseasonal flows. The composite is shown on every three day average, and only the centered day is marked in each panel for simplicity. For example, day 0

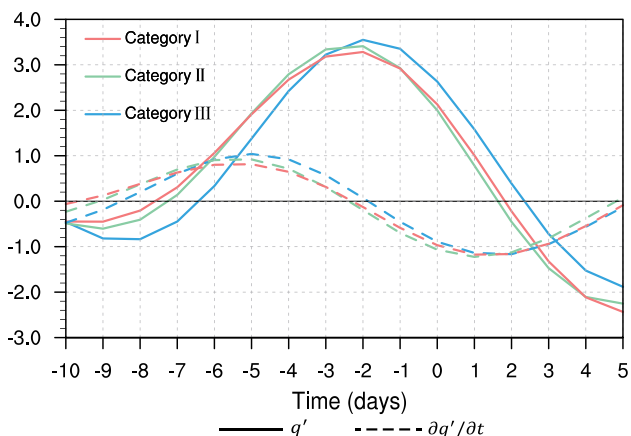


Fig. 5 Evolutions of boundary-layer (1000–850 hPa) integrated intraseasonal moisture anomaly (solid, $10^{-1} \text{ kg m}^{-2}$) and its tendency (dashed, $10^{-1} \text{ kg m}^{-2} \text{ day}^{-1}$) averaged over SC (22–30° N, 110–120° E) from day -10 to day +5 for Category I (red), II (green) and III (blue)

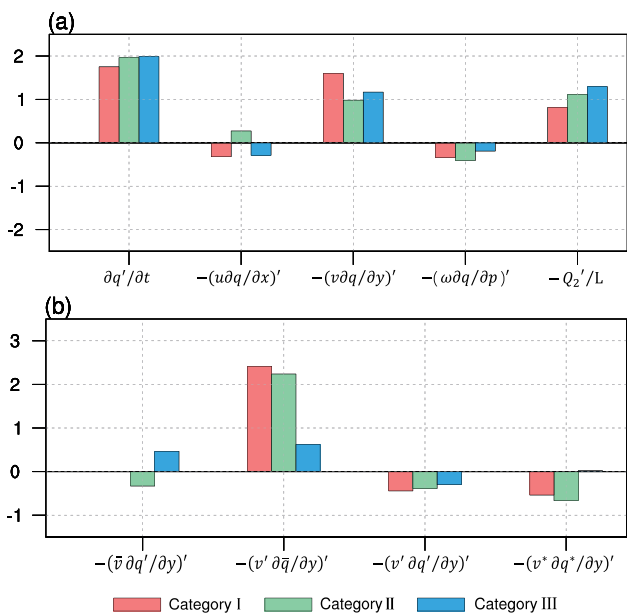


Fig. 6 a Boundary-layer integrated intraseasonal moisture budget terms over SC (22–30° N, 110–120° E) averaged over days -7 to -5. From left to right, specific humidity tendency, zonal moisture advection, meridional moisture advection, vertical moisture advection and moisture sink. **b** Individual components of the moisture meridional advection process. Unit is $10^{-1} \text{ kg m}^{-2} \text{ day}^{-1}$

denotes the average from day -1 to day +1. Note that day -6, denoting the average over day -7 to day -5, is the BL moistening phase and is the focus.

We first examine the circulation evolutions associated with Category I. Figure 7 presents horizontal evolutions of intraseasonal 850-hPa wind and geopotential height

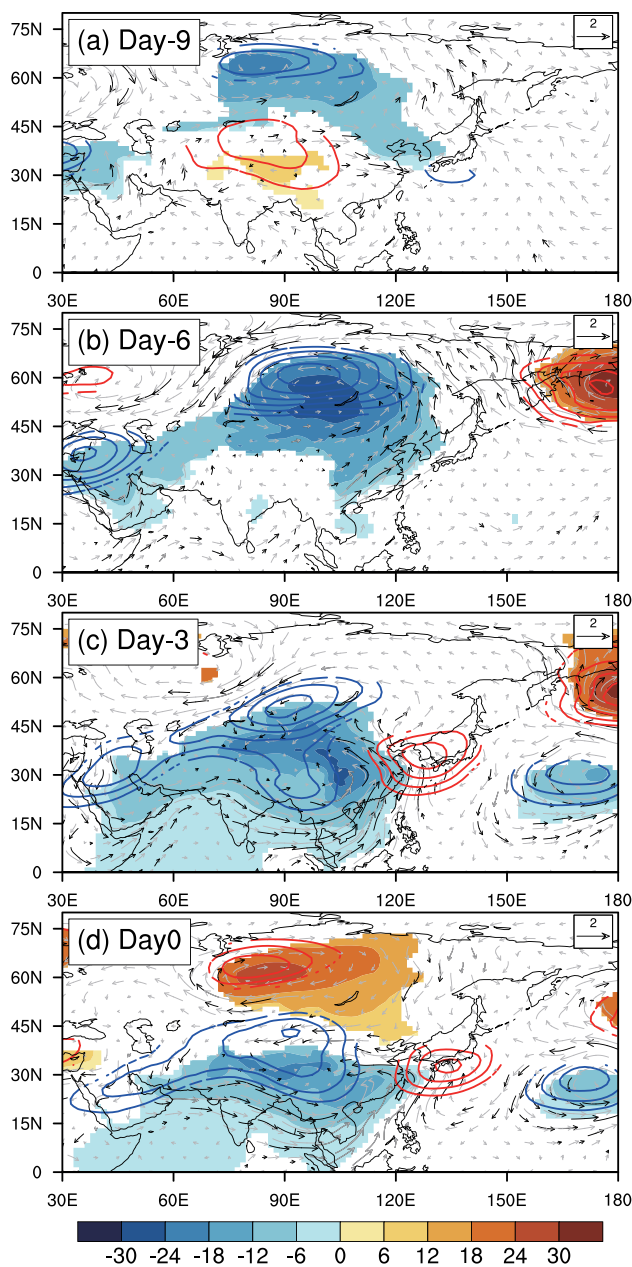


Fig. 7 Horizontal evolutions of 850-hPa intraseasonal geopotential height anomalies (shading, gpm) and 500-hPa intraseasonal geopotential height anomalies (contour with interval of 6 gpm) and wind anomalies (vector, m s^{-1}) from day -9 to day 0 for Category I. Regions where composite wind (geopotential height) anomalies are significant at 90% level are denoted by black vectors (colors)

anomalies as well as 500-hPa geopotential height anomalies. On day -9, a significant low-level cyclonic anomaly is seen over the northern Asia, with a center near 65° N, 85° E (Fig. 7a). It shows a quasi-barotropic vertical structure, albeit with a northward tilt with height to some extent. The cyclone then strengthens and moves southeastward,

showing its lower-level center near 55° N, 105° E and the middle-level center near 60° N, 95° E on day -6 (Fig. 7b). It is noticed that a significant southwesterly in lower troposphere emerges over SC during this period, and such wind is closely related to the mid-latitude cyclone. During the wet phase of SC (Fig. 7c and d), the southwesterly wind near SC is reinforced, which could further facilitate moisture transport and strengthening and maintaining precipitation. This may be partly due to the positive feedback from precipitation (e.g., Cheng et al. 2021).

Figure 8 displays the lagged time-latitude evolution of intraseasonal geopotential height anomaly at 850 hPa along $80\text{--}120^{\circ}$ E from day -20 to day $+10$ for Category I. A low-pressure anomaly is clearly seen propagating southward continuously from higher latitude toward lower latitude, which is consistent with Yao et al. (2020).

Unlike Category I the other two categories are closely related to the MJO in tropics, so their horizontal evolutions of 850-hPa wind and stream function anomalies as well as tropical OLR anomalies are presented. For Category II (Fig. 9), a zonally elongated weak suppressed convective anomaly is seen near the equator from the MC to the WP on day -9 ; its center shifts eastward into the WP on day -6 , while an enhanced convective anomaly emerges over the western IO. Such zonal dipole convective structure propagates eastward continuously and reach the maximum amplitude near day 0, when the wet (dry) center is over the eastern IO (WP). Then the intensity of convection anomalies decay as they move on in the following days.

In association with the eastward propagating MJO suppressed convection, a pair of anticyclonic gyres straddling the equator as the Gill-Matsuno response (Gill 1980) to the equatorial suppressed convection is also clearly seen moving eastward. The averaged longitude location for the

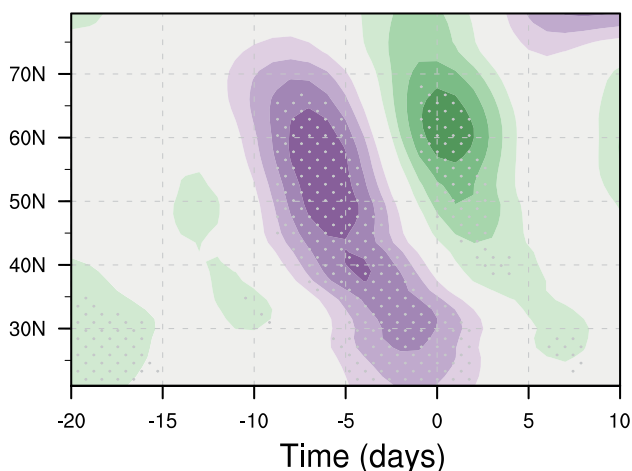


Fig. 8 Latitude-time evolution of 850-hPa intraseasonal geopotential height anomalies (gpm) along $80\text{--}120^{\circ}$ E for Category I. The regions exceeding the 95% confidence level are stippled

anticyclone centers in both hemisphere is near 80° E on day -9 , and shifts to 125° E on day -6 . When the MJO convection matures near day 0, the longitude location of the anticyclone centers are very close to that of the suppressed convection (Zhang and Ling 2012). Note that during the moistening phase (day -6), a prominent southwesterly wind begin to influence SC, which is closely related to the anticyclone over the northwestern Pacific (NWP). From day -3 to day 0, the southwesterly wind is reinforced, partly due to enhancement of the MJO suppressed convection over the equatorial WP and partly to the positive feedback from precipitation over SC. After day $+1$, as the anticyclone moves eastward with the MJO suppressed convection, the wind signal over SC is not clear. To sum up, the appearance of low-level southerly wind in the moistening phase for Category II is related to the anticyclone over the NWP, which is in response to the MJO suppressed convection over the equatorial WP.

For Category III (Fig. 10), the MJO enhanced convection is observed near the central IO (80° E) on day -9 , that extends eastward to the eastern IO on day -6 . It attains the peak amplitude on day 0, and decays afterwards as slowly moving eastward. It is noted that the main body of the MJO enhanced convection detours to the south of the equator when it crosses over the MC from day -3 to day $+3$. Such propagation feature of the slow-propagating MJO is in contrast to that of the fast-propagating MJO (Xiang et al. 2022).

In response to the MJO enhanced convection, a pair of cyclonic gyres straddles the equator to the west of it and moves eastward in pace with it. As one can see, the center of the northern-hemisphere cyclone is near the Arabian Sea on day -9 , shifts to the eastern India on day -6 and over the Indochina Peninsula from day -3 . It is clear that SC begins to be influenced by weak southwesterly wind on day -6 , which is associated with the cyclone over the India. During day -3 to day 0, the southerly wind is reinforced partly due to the enhancement of MJO enhanced convection and partly due to the positive feedback from SC precipitation. To sum up, the appearance of low-level southerly wind in the moistening phase for Category III is related to the cyclone centered over India, which is a response to the MJO enhanced convection over the eastern IO.

As the low-level southerly winds that induce BL moistening are associated with distinct large-scale circulations, it is speculated that the moisture origins may be also different. Figure 11 displays the vertically integrated (1000–300 hPa) water vapor flux averaged over day -7 to day -5 in each category. In general, the moisture fluxes resemble the low-level wind patterns. For Category I, the southwesterly over SC is directly connected to the southerly over the South China Sea (SCS). For Category II, prominent easterly is seen in the tropical area, and it turns into southerly over SC, which is consistent with the low-level anticyclone over the WNP. For Category III,

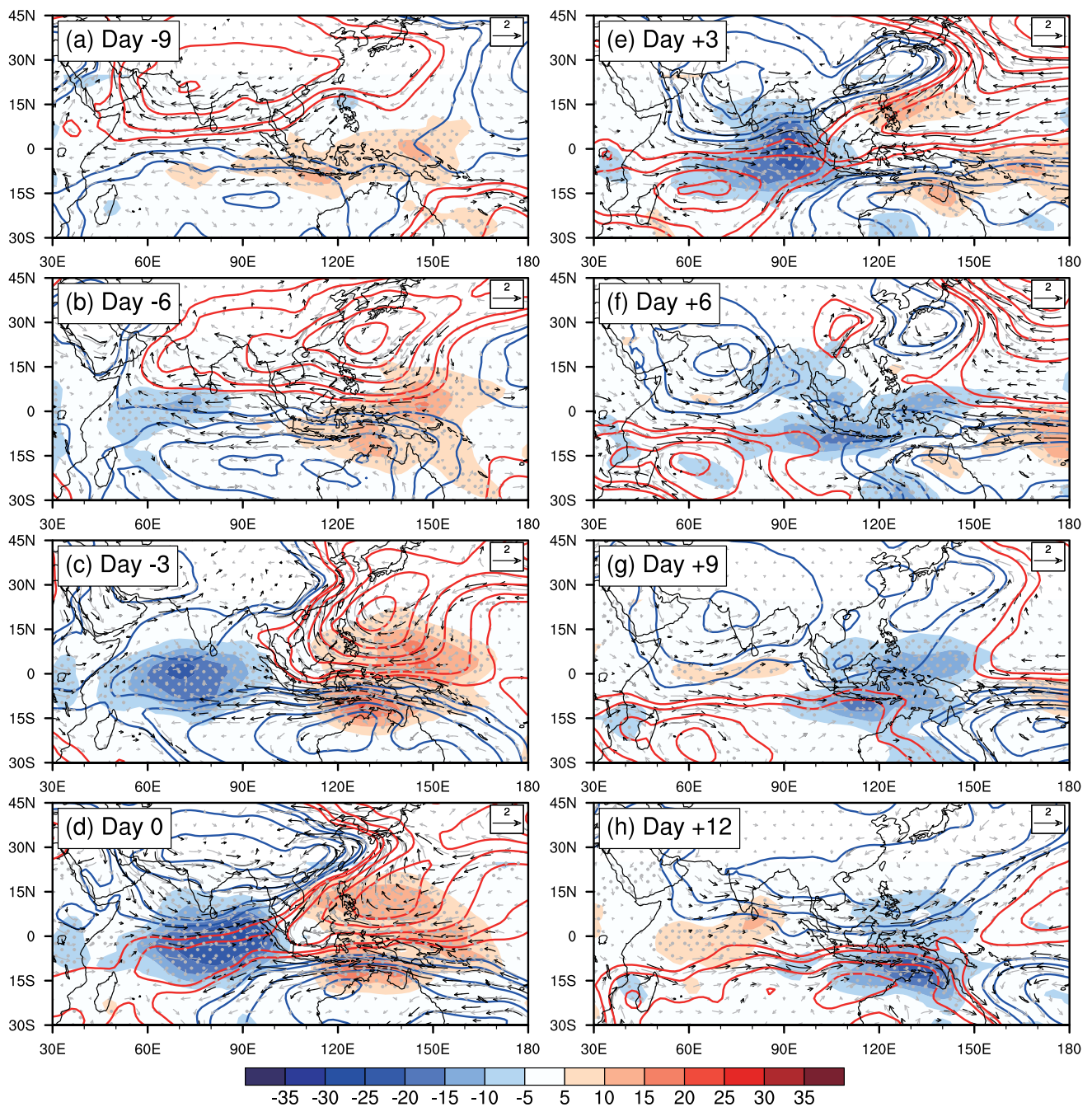


Fig. 9 Horizontal evolutions of intraseasonal OLR anomalies (shading, $W m^{-2}$), 850-hPa intraseasonal streamfunction anomalies (contour with interval of $6.0 \times 10^5 m^2 s^{-1}$) and wind anomalies (vector,

$m s^{-1}$) from day - 9 to day + 12 for Category II. Regions where composite wind (OLR) anomalies are significant at 90% level are denoted by black vectors (dots)

southwesterly is seen over the BOB, which extends north-eastward across the Indochina Peninsula to SC; this is in contrast to Category I, which shows strong southwesterly over BOB but no signal of flux over the Indochina Peninsula. The above results suggest that the water vapor over SC during the moistening phase stems from different ocean regions; they are the SCS, WNP and BOB for the three categories, respectively.

6 Conclusions and discussion

In boreal winter, the SC precipitation witnesses strong intraseasonal variabilities, which are closely related to atmospheric intraseasonal oscillations. But the subseasonal prediction skill for it is very low in current state-of-the-art forecasting systems. It may be partially due to lack of understanding the critical intraseasonal circulation

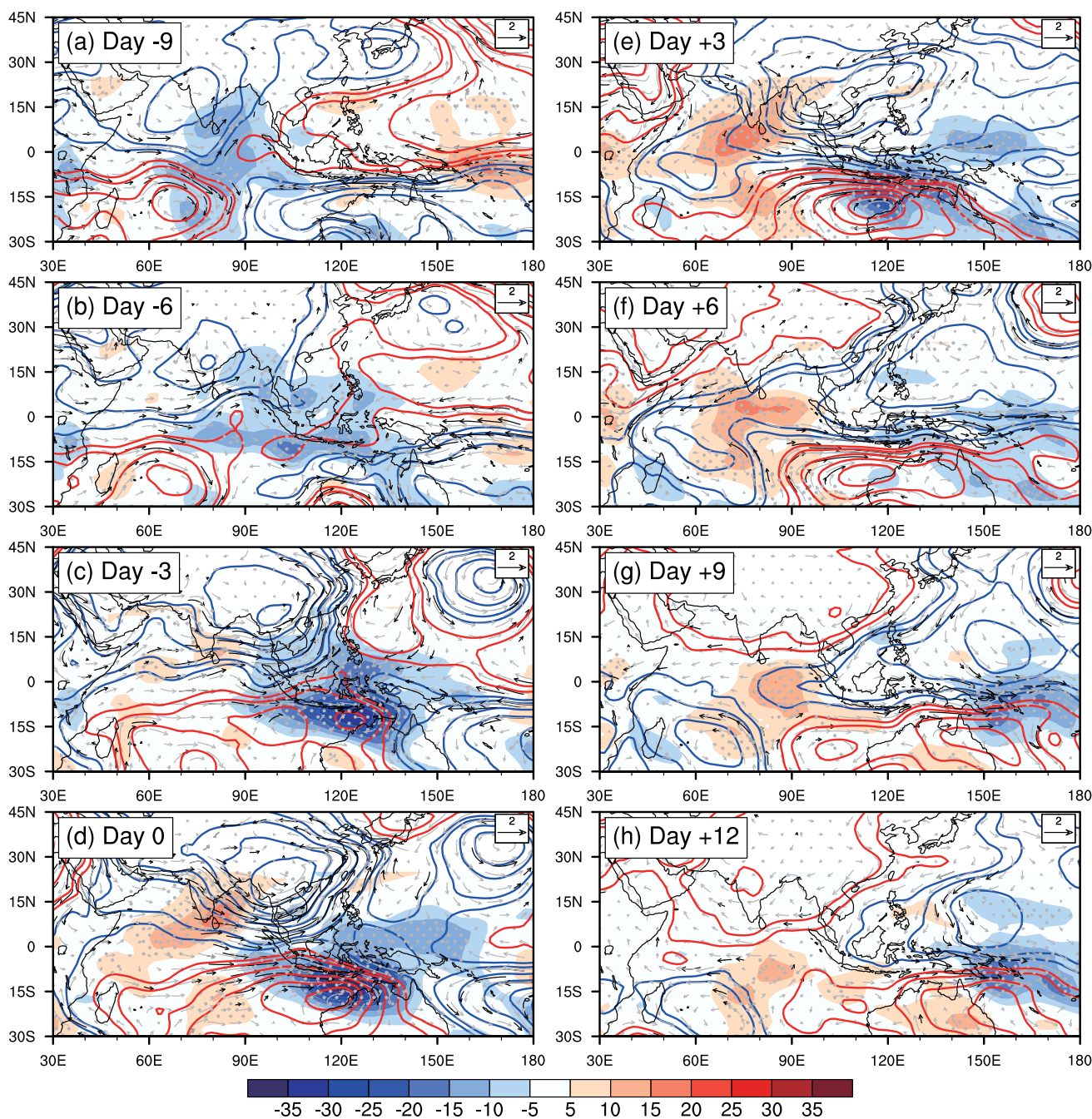


Fig. 10 Same as Fig. 9, but for Category III

systems and the related impacting mechanisms. Some previous studies reported that the MJO life cycle could significantly modulate the SC precipitation, whereas more recent studies identified crucial impacts from the middle- and high-latitude ISOs, in particular through inducing a southward propagating low-level cyclonic (anticyclonic)

anomaly from polar regions. It suggests the diversity of intraseasonal circulations that induce intraseasonal precipitation events (IPEs) over SC, which yet to be studied systematically. The current study investigates this issue by analyzing the SC enhanced IPEs during boreal winter (November–March) in 1979–2016.

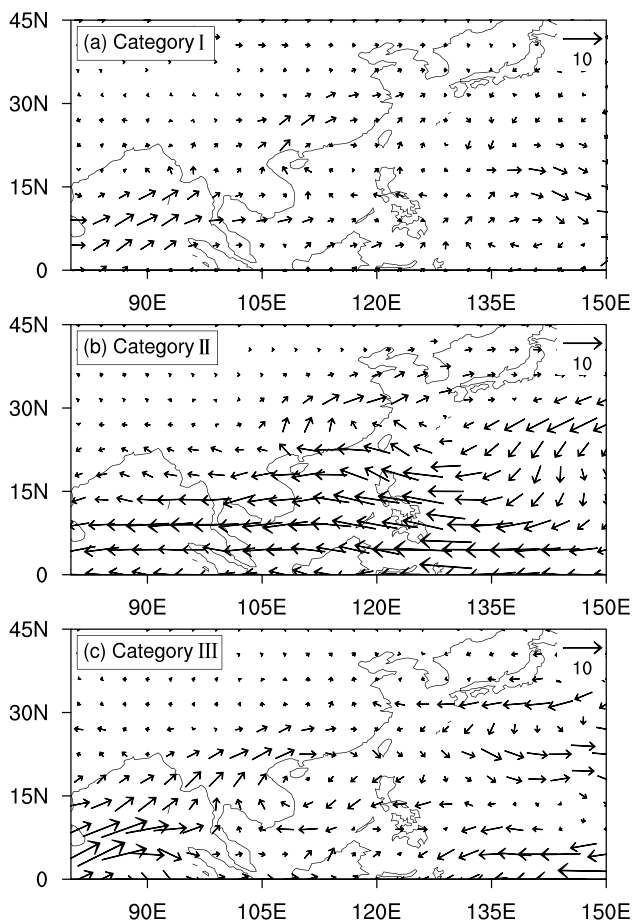


Fig. 11 Column (1000–300 hPa) integrated intraseasonal water vapor transport ($\text{kg m}^{-1} \text{s}^{-1}$) averaged from day - 7 to day - 5 for **a** Category I, **b** Category II and **c** Category III

Firstly, a total of 144 IPEs were categorized by applying *k*-means clustering analysis to the spatial distribution of intraseasonal OLR anomalies over the Indo-western Pacific Ocean near day 0 that denotes the peak wet phase. They can be optimally classified into four groups, with proportions of roughly 45%, 33%, 14% and 8% from top to bottom. Note that the last three groups are derived directly from the *k*-means clustering analysis while the first group is comprised of those non-clustered events. The current study mainly investigates the top three groups that account for the majority, referring to be Category I, II and III respectively, whereas the last group with the least proportion is omitted. The three groups exhibit similar precipitation evolutions where day - 4 is the onset day of rainfall, but the related tropical convection anomalies are distinguishable. In Category I, no clear signal of MJO in tropics is observed, but an intraseasonal cyclonic anomaly with quasi-barotropic vertical structure propagates southward continuously from the northern Asia. Category II is featured by a fast-propagating MJO which shows enhanced (suppressed) convective

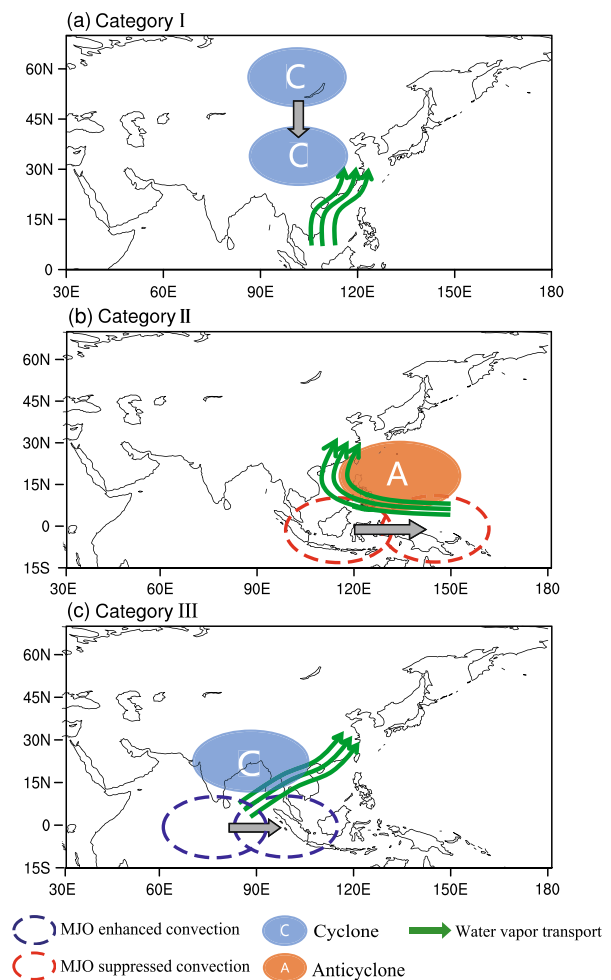


Fig. 12 Schematic diagrams showing the dominant intraseasonal circulation anomalies that induce SC intraseasonal precipitation anomalies during the moistening phase for **a** Category I, **b** Category II and **c** Category III. The filled blue (orange) circle indicates low-level cyclone (anticyclone), the blue (red) circle the MJO enhanced (suppressed) convection, and the green vectors the water vapor transport

anomalies over the IO (WP) on day 0. Category III is characterized by a slow-propagating MJO that exhibits enhanced convective anomalies near the MC on day 0.

For each category, the BL moistening prior to the onset of precipitation (day - 7 to day - 5) acts as an essential component that leads to rainfall. Through an intraseasonal moisture budget analysis, it is found that the three categories commonly involve two dominant processes for the BL moistening: the advection of basic state moisture by intraseasonal southerly wind and $-(\frac{Q_2}{L})$. They show comparable contributions while the latter is related to local descending motion.

The low-level southerly winds in each category that is crucial for moisten the BL over SC prior to the onset of precipitation are derived from distinct large-scale circulation systems, which are summarized in schematic diagrams

of Fig. 12. In Category I, the southerly wind over SC arises from the southwesterly to the southeast of the mid-latitude cyclone that propagates from the northern Asia southward. In Category II, it is attributed to the southwesterly to the west of the anticyclonic gyre over the NWP in response to the MJO suppressed convection over the equatorial WP. In Category III, it is related to the southwesterly to the east of the cyclonic gyre centered near the Indian continent as a response to the MJO enhanced convection over the equatorial eastern IO. For Category II (III), the MJO suppressed (enhanced) convection shifts eastward from the Maritime Continent to the western Pacific (from the central IO to the eastern IO). Furthermore, the water vapor that moistens SC is transported from different regions. The primary moisture origins are the South China Sea for Category I, the northwestern Pacific Ocean for Category II and the Bay of Bengal for Category III. The results shed light on diverse initiation mechanisms for enhanced IPEs over SC and have implications for improving the sub-seasonal prediction of SC precipitation.

It should be mentioned that the current study suggests comparable contributions from the MJO and the middle-and-high-latitude ISO to the enhanced SC IPEs, as Categories II and III denoting the MJO impacts account for 47% of the total and Category I representing the middle-and-high-latitude ISO influence accounts for 45%; whereas some previous studies emphasized the dominant role of the middle-and-high-latitude ISO (e.g., Yao et al. 2015, 2020). The underestimated MJO influence may be due to that conventional analyzing methods used in previous studies are difficult to identify impacts from different MJO types.

Although the positive contribution from MJO phases 2–3 to the enhanced SC intraseasonal precipitation anomaly has been revealed extensively, that from MJO phases 4–5 as shown in Category III events has been seldomly reported. A recent study by Chen et al. (2020) revealed an MJO–SC precipitation relationship similar to our Category III events. However, their results are only evident in El Niño winters, whereas the Category III events detected in this study do not show interannual preference (figure not shown). The discrepancy may be due to the different days for composite, as those in Chen et al. (2020) were based on MJO events but are based on enhanced SC IPEs in current study.

There are several other issues that are not addressed here. For instance, we have suggested different extratropical impacts from fast and slow MJOs; nevertheless, why different propagation speeds of the MJO could induce distinguished extratropical circulations remains unclear. It is also worthy of investigation that why the low-level anticyclone gyres propagate in pace with the suppressed MJO convection but the cyclone gyres are loosely tied to the MJO enhanced convection for the fast MJO (Fig. 9), while the opposite is found in the slow MJO (Fig. 10).

Acknowledgements This work was supported by National Natural Science Foundation of China (42088101 and 41975108), NOAA grant NA18OAR4310298 and NSFC-Shandong Joint Fund for Marine Science Research Centers (U1606405), Jiangsu College Students' innovation and entrepreneurship training program (202210300066z).

Author contributions LW designed the original ideas presented in this manuscript. JJ, XZ and ZC conducted the analysis. LW and JJ interpreted the results and wrote the manuscript. TL participated in improvement of the manuscript. All authors read and approved the final manuscript.

Data availability The data analyzed in this study are available from the author upon reasonable request.

Declarations

Conflict of interest The authors have no relevant financial or non-financial interests to disclose.

References

- Chen X, Li C, Li X, Yang M, Li L (2020) Modulation of the impacts of Madden–Julian Oscillation on winter rainfall in China by El Niño–Southern Oscillation. *Int J Climatol* 40:4039–4052. <https://doi.org/10.1002/joc.6437>
- Chen X, Ling J, Li C et al (2021a) Different impacts of Madden–Julian oscillation on winter rainfall over southern China. *J Meteorol Res* 35:271–281. <https://doi.org/10.1007/s13351-021-0138-7>
- Chen Y-L, Sui C-H, Chang C-P, Tseng K-C (2021b) Effect of the MJO on East Asian winter rainfall as revealed by an SVD analysis. *J Clim*. <https://doi.org/10.1175/JCLI-D-20-0941.1>
- Cheng Y, Wang L, Li T (2021) Two distinct types of 10–30-day persistent heavy rainfall events over the Yangtze River Valley. *J Clim* 34:9571–9584. <https://doi.org/10.1175/JCLI-D-20-0741.1>
- Cui, J.-X., T. Li (2021) Changes in MJO characteristics and impacts in the past century. *J Clim* (**in press**)
- Dee DP, Uppala SM, Simmons AJ et al (2011) The ERA-Interim reanalysis: configuration and performance of the data assimilation system. *Q J R Meteorological Soc* 137:553–597. <https://doi.org/10.1002/qj.828>
- Duchon CE (1979) Lanczos filtering in one and two dimensions. *J Appl Meteorol Climatol* 18:1016–1022
- Gill AE (1980) Some simple solutions for heat-induced tropical circulation. *Q J R Meteorol Soc* 106:447–462
- He J, Lin H, Wu Z (2011) Another look at influences of the Madden–Julian Oscillation on the wintertime East Asian weather. *J Geophys Res* 116:D03109. <https://doi.org/10.1029/2010JD014787>
- Hong C-C, Li T (2009) The extreme cold anomaly over Southeast Asia in February 2008: roles of ISO and ENSO*. *J Clim* 22:3786–3801. <https://doi.org/10.1175/2009JCLI2864.1>
- Hsu P, Li T (2012) Role of the boundary layer moisture asymmetry in causing the eastward propagation of the Madden–Julian Oscillation*. *J Clim* 25:4914–4931. <https://doi.org/10.1175/JCLI-D-11-00310.1>
- Hung C, Lin H-J, Hsu H-H (2014) Madden–Julian oscillation and the winter rainfall in Taiwan. *J Clim* 27:4521–4530. <https://doi.org/10.1175/JCLI-D-13-00435.1>
- Jeong J-H, Kim B-M, Ho C-H, Noh Y-H (2008) Systematic variation in wintertime precipitation in East Asia by MJO-induced extratropical vertical motion. *J Clim* 21:788–801. <https://doi.org/10.1175/2007JCLI1801.1>

- Jia X, Chen L, Ren F, Li C (2011) Impacts of the MJO on winter rainfall and circulation in China. *Adv Atmos Sci* 28:521–533. <https://doi.org/10.1007/s00376-010-9118-z>
- Kim S, Kug J-S, Seo K-H (2020) Impacts of MJO on the intraseasonal temperature variation in East Asia. *J Clim* 33:8903–8916. <https://doi.org/10.1175/JCLI-D-20-0302.1>
- Li C, Ling J, Song J et al (2014) Research progress in China on the tropical atmospheric intraseasonal oscillation. *J Meteorol Res* 28:671–692
- Li T, Ling J, Hsu P-C (2020) Madden–Julian oscillation: its discovery, dynamics, and impact on East Asia. *J Meteorol Res* 34:20–42
- Liebmann B, Smith CA (1996) Description of a complete (interpolated) outgoing longwave radiation dataset. *Bull Am Meteorol Soc* 77:1275–1277. [https://doi.org/10.1175/1520-0477\(1996\)077<1255:EA>2.0.CO;2](https://doi.org/10.1175/1520-0477(1996)077<1255:EA>2.0.CO;2)
- Liu D, Yang X (2010) Mechanism responsible for the impact of Madden-Julian Oscillation on the wintertime rainfall over eastern China. *Scientia Meteorologica Sinica* 5
- Liu F, Ouyang Y, Wang B et al (2020) Seasonal evolution of the intraseasonal variability of China summer precipitation. *Clim Dyn*. <https://doi.org/10.1007/s00382-020-05251-0>
- Liu F, Wang B, Ouyang Y et al (2022) Intraseasonal variability of global land monsoon precipitation and its recent trend. *NPJ Clim Atmos Sci*. <https://doi.org/10.1038/s41612-022-00253-7> (In Press)
- Madden RA, Julian PR (1972) Description of global-scale circulation cells in the tropics with a 40–50 day period. *J Atmos Sci* 29:1109–1123
- Park T-W, Ho C-H, Deng Y (2014) A synoptic and dynamical characterization of wave-train and blocking cold surge over East Asia. *Clim Dyn* 43:753–770. <https://doi.org/10.1007/s00382-013-1817-6>
- Peng J, Dadson S, Leng G et al (2019) The impact of the Madden–Julian Oscillation on hydrological extremes. *J Hydrol* 571:142–149
- Ren H-L, Ren P (2017) Impact of Madden–Julian Oscillation upon winter extreme rainfall in Southern China: observations and predictability in CFSv2. *Atmosphere* 8:192. <https://doi.org/10.3390/atmos8100192>
- Seo K-H, Lee H-J, Frierson DMW (2016) Unraveling the teleconnection mechanisms that induce wintertime temperature anomalies over the Northern Hemisphere continents in response to the MJO. *J Atmos Sci* 73:3557–3571. <https://doi.org/10.1175/JAS-D-16-0036.1>
- Stan C, Straus DM, Frederiksen JS et al (2017) Review of tropical-extratropical teleconnections on intraseasonal time scales: the subseasonal to seasonal (S2S) teleconnection sub-project. *Rev Geophys* 55:902–937. <https://doi.org/10.1002/2016RG000538>
- Tao S, Wei J (2008) Severe snow and freezing-rain in January 2008 in the southern China. *Clim Environ Res* 13:337–350
- Wang T, Yang S, Wen Z, et al (2011) Variations of the winter India–Burma Trough and their links to climate anomalies over southern and eastern Asia. *J Geophys Res Atmos* 116
- Wang B, Chen G, Liu F (2019) Diversity of the Madden-Julian Oscillation. *Sci Adv* 9. <https://doi.org/10.1126/sciadv.aax0220>
- Wheeler MC, Hendon HH (2004) An all-season real-time multivariate MJO Index: development of an index for monitoring and prediction. *Mon Weather Rev* 132:1917–1932. [https://doi.org/10.1175/1520-0493\(2004\)132%3c1917:AARMMI%3e2.0.CO;2](https://doi.org/10.1175/1520-0493(2004)132%3c1917:AARMMI%3e2.0.CO;2)
- Wu J, Gao XJ (2013) A gridded daily observation dataset over China region and comparison with the other datasets (in Chinese). *Chin J Geophys Chin Ed* 56:1102–1111. <https://doi.org/10.6038/cjg20130406>
- Wu J, Yuan Z, Qian Y, Liang C (2009) The role of intraseasonal oscillation in the southern-China snowstorms during January 2008. *J Trop Meteor* 25:103–112
- Xiang B, Coauthors (2022) S2S prediction in GFDL SPEAR: MJO diversity and teleconnections. *Bull Am Meteor Soc* 103:E463–E484. <https://doi.org/10.1175/BAMS-D-21-0124.1>
- Yao S, Huang Q (2016) An analysis of extreme intraseasonal rainfall events during January–March 2010 over eastern China. *Dyn Atmos Oceans* 75:22–32. <https://doi.org/10.1016/j.dynatmoce.2016.04.001>
- Yao S, Huang Q, Li T, Zhang C (2014) The intraseasonal oscillations of precipitation and circulations from January to March in 2010 in East Asia. *Meteorol Atmos Phys* 123:67–79
- Yao Y, Lin H, Wu Q (2015) Subseasonal Variability of Precipitation in China during Boreal Winter. *J Clim* 28:6548–6559. <https://doi.org/10.1175/JCLI-D-15-0033.1>
- Yao S, Tong Q, Li T, Gong K (2020) The 10–30-day oscillation of winter rainfall in southern China and its relationship with circulation patterns in different latitudes. *Int J Climatol* 40:3268–3280. <https://doi.org/10.1002/joc.6396>
- Zhang C (2013) Madden–Julian oscillation: bridging weather and climate. *Bull Am Meteorol Soc* 94:1849–1870. <https://doi.org/10.1175/BAMS-D-12-00026.1>
- Zhang C, Ling J (2012) Potential vorticity of the Madden–Julian oscillation. *J Atmos Sci* 69:65–78. <https://doi.org/10.1175/jas-d-11-081.1>
- Zhu T, Yang J (2021) Two types of mid-high-latitude low-frequency intraseasonal oscillation near Ural Mountain in boreal summer. *J Clim*. <https://doi.org/10.1175/JCLI-D-20-0589.1>
- Zong H, Bueh C, Ji L (2014) Wintertime extreme precipitation event over southern China and its typical circulation features. *Chin Sci Bull* 59:1036–1044. <https://doi.org/10.1007/s11434-014-0124-x>

Publisher's Note Springer Nature remains neutral with regard to jurisdictional claims in published maps and institutional affiliations.

Springer Nature or its licensor holds exclusive rights to this article under a publishing agreement with the author(s) or other rightsholder(s); author self-archiving of the accepted manuscript version of this article is solely governed by the terms of such publishing agreement and applicable law.